JGR Planets

RESEARCH ARTICLE
10.1029/2018JE005739

Overturn of Ilmenite-Bearing Cumulates in a Rheologically Weak Lunar Mantle

Shuoran Yu[1], Nicola Tosi[2,3], Sabrina Schwinger[2], Maxime Maurice[2], Doris Breuer[2], and Long Xiao[1,4]

[1]State Key Laboratory of Lunar and Planetary Sciences, Macau University of Science and Technology, Macau SAR, China, [2]Institute of Planetary Research, German Aerospace Center (DLR), Berlin, Germany, [3]Department of Astronomy and Astrophysics, Berlin Institute of Technology, Berlin, Germany, [4]Planetary Science Institute, China University of Geosciences, Wuhan, China

Key Points:
- We computed the crystallization sequence of the lunar magma ocean to simulate the overturn of ilmenite-bearing cumulates
- Stagnant lid formation prevents the overturn unless the reference viscosity at 1600 K is 10^{20} Pa s or lower
- Independent of the rheological parameters, ilmenite cumulates sink as small-scale diapirs

Correspondence to:
S. Yu,
shuoran.yu@icloud.com

Citation:
Yu, S., Tosi, N., Schwinger, S., Maurice, M., Breuer, D., & Xiao, L. (2019). Overturn of ilmenite-bearing cumulates in a rheologically weak lunar mantle. *Journal of Geophysical Research: Planets*, *124*, 418–436. https://doi.org/10.1029/2018JE005739

Received 30 JUN 2018
Accepted 25 JAN 2019
Accepted article online 31 JAN 2019
Published online 18 FEB 2019

Abstract The crystallization of the lunar magma ocean (LMO) determines the initial structure of the solid Moon. Near the end of the LMO crystallization, ilmenite-bearing cumulates (IBC) form beneath the plagioclase crust. Being denser than the underlying mantle, IBC are prone to overturn, a hypothesis that explains several aspects of the Moon's evolution. Yet the formation of stagnant lid due to the temperature dependence of viscosity can easily prevent IBC from sinking. To infer the rheological conditions allowing IBC to sink, we calculated the LMO crystallization sequence and performed high-resolution numerical simulations of the overturn dynamics. We assumed a diffusion creep rheology and tested the effects of reference viscosity, activation energy, and compositional viscosity contrast between IBC and mantle. The overturn strongly depends on reference viscosity and activation energy and is facilitated by a low IBC viscosity. For a reference viscosity of 10^{21} Pa s, characteristic of a dry rheology, IBC overturn cannot take place. For a reference viscosity of 10^{20} Pa s, the overturn is possible if the activation energy is a factor of 2–3 lower than the values typically assumed for dry olivine. These low activation energies suggest a role for dislocation creep. For lower-reference viscosities associated with the presence of water or trapped melt, more than 95% IBC can sink regardless of the activation energy. Scaling laws for Rayleigh-Taylor instability confirmed these results but also showed the need of numerical simulations to accurately quantify the overturn dynamics. Whenever IBC sink, the overturn occurs via small-scale diapirs.

Plain Language Summary The accretion of the debris resulting from the giant collision that formed the Earth-Moon system caused the formation of a deep lunar magma ocean. The initial composition profile of the Moon results from the solidification of this magma ocean. One of the late solidification products is a thin layer containing ilmenite, which is highly enriched in titanium and forms over a depth of about 40–80 km. This layer is much denser than the underlying mantle, it tends thus to overturn and sink toward the core. The overturn hypothesis explains several features of the evolution of the Moon. However, the strong temperature dependence of the viscosity makes the part of the mantle where this titanium-rich layer solidifies very stiff and its overturn very difficult. In this work, we used numerical simulations to infer which deformation properties the mantle needs to have for the overturn to be possible. We found that the overturn requires a significantly weaker and less temperature dependent viscosity than usually thought. The required low viscosity and its weak temperature dependence can be explained by the presence of water and residual melt in the Moon and/or by the effects of nonlinear deformation dependent both on temperature and stress.

1. Introduction

Crystallization models of the lunar magma ocean (LMO) indicate that after the formation of a primordial crust by plagioclase flotation, ilmenite-bearing cumulates (IBC) containing Ti-rich oxides form when 87–95 vol.% of the mantle has solidified (e.g., Elardo et al., 2011; Elkins-Tanton et al., 2011; Snyder et al., 1992). With a density of more than 3,700 kg/m^3 (Elkins-Tanton et al., 2002), IBC are significantly denser than the underlying olivine- and pyroxene-rich mantle, hence gravitationally unstable and prone to overturn.

The hypothesis of the overturn of the LMO was first put forth by Ringwood and Kesson (1976) to interpret the origin of high-Ti basalts detected on the lunar nearside. After sinking to the core-mantle boundary (CMB),

IBC, being also highly enriched in heat-producing elements, are thought to heat up, rise buoyantly through the mantle, and undergo partial melting, providing thus a source for Ti-rich surface basalts (e.g., Hess & Parmentier, 1995). In addition, the extensive volcanic units on the lunar nearside, the so-called Procellarum KREEP Terrane, have been hypothesized to be the consequence of a degree-one upwelling of ilmenite-rich material rising from the CMB (Zhang et al., 2013a; Zhong et al., 2000). Cooling of the core induced by upwelling IBC may have been at the origin of an early lunar dynamo (Cisowski et al., 1983; Shea & Fuller, 2012; Stegman et al., 2003). Furthermore, overturned IBC may also be responsible for the low-viscosity zone inferred to be present above the CMB (Harada et al., 2014; Weber et al., 2011).

Although the hypothesis of the IBC overturn provides a suitable explanation for several aspects of lunar evolution, it still poses a problem related to the dynamics of the overturn itself. At the relatively low temperatures at which IBC crystallize, the rapid formation of the stagnant lid—the cold and stiff part on the uppermost mantle—can easily prevent these cumulates from sinking downward (Elkins-Tanton et al., 2002; Van Orman & Grove, 2000). As a consequence, IBC would remain permanently trapped in a highly viscous layer beneath the plagioclase crust, rendering it difficult to invoke the overturn of late-stage, Ti-rich cumulates as a possible explanation for the issues described above.

Indeed, theoretical models of the interior evolution of the Moon often use initial conditions that reflect a compositional configuration subsequent to the IBC overturn, which is implicitly assumed to take place despite the difficulties related to the formation of the stagnant lid (e.g., Evans et al., 2014; Stegman et al., 2003; Zhang et al., 2013a, 2013b, 2017). An exception to this simplified approach is the work by de Vries et al. (2010) who modeled the overturn of IBC using a diffusion creep rheology based on the linearized form of the Arrhenius law, the Frank-Kamenetzkii approximation. However, it is well known that under this approximation the strong viscosity gradients delivered by the more realistic Arrhenius law are drastically reduced (e.g., Stein & Hansen, 2013). The effective viscosity of near-surface layers obtained using the Frank-Kamenetzkii approximation is much smaller, with the consequence that the mobilization of the IBC, and possibly even of the bottom of the crust, is strongly facilitated.

Assessing the conditions under which the overturn of IBC can take place is thus critical to understand the role of late-stage cumulates in the lunar evolution. Here we analyze this problem by using a strongly temperature-dependent Arrhenius law for diffusion creep and investigate its effects on the development of the IBC overturn.

2. Methods

2.1. Crystallization of the LMO

We modeled the crystallization of the LMO in spherical geometry using the alphaMELTS software (Ghiorso et al., 2002; Smith & Asimow, 2005). Assuming the lunar core to have a composition ranging from pure Fe to Fe-FeS, its radius has been estimated to be between 200 and 530 km (Hood & Jones, 1987; Kuskov & Kronrod, 2001; Kuskov et al., 2002; Weber et al., 2011). In this study, we considered a core radius of 390 km (e.g., Laneuville et al., 2013) and a whole-mantle magma ocean occupying a spherical shell with a depth of 1,350 km. This core radius was chosen in order to match the density of the Moon based on the assumed magma ocean composition (see below). The variability of the maximum magma ocean depth resulting from the uncertainty of the core size is too small to cause significant changes in the bulk mineralogy of the magma ocean cumulates, especially at the final stages of IBC crystallization. Some studies suggest that a density discontinuity at a depth of 500–600 km specifies the bottom of LMO, but it is still unknown whether or not this feature is ubiquitous (Wieczorek et al., 2006).

We assumed a purely fractional crystallization by cooling the magma ocean in temperature steps of 1 K with the retention of 5% trapped liquid (e.g., Elkins-Tanton et al., 2011). Note that the amount of trapped liquid does not significantly change the IBC thickness and bulk composition. We also assumed a constant oxygen fugacity set at one log-10 unit below the Iron-Wüstite buffer (IW-1). This value lies within the range from IW to IW-2 estimated for the Moon on the base of the composition of mare basalts (Wadhwa, 2008). Deviations of 1 order of magnitude from the average IW-1 throughout the crystallization history of the magma ocean do not significantly affect the calculated bulk mineralogy or thickness of the IBC, so that they can be ignored for the scope of this study.

We used a starting bulk composition with main oxide content as proposed by O'Neill (1991) but an elevated TiO_2 content of 0.4 wt.% corresponding to the maximum estimates of other authors (Buck & Toksoez, 1980;

Elkins-Tanton et al., 2011; Morgan et al., 1978; Snyder et al., 1992). This choice tends to maximize the thickness of the resulting IBC layer (36 km as shown in section 3.1), which can then be properly resolved with the mesh of our numerical model. Using the minimum estimate (0.17%) for the TiO_2 content would reduce the thickness of the IBC layer by about 10%. The bulk content of the heat-producing elements U, Th, and K was set according to the estimate proposed by Taylor (1982).

All solids, except plagioclase, formed in a given temperature step were assumed to instantaneously form a cumulate at the bottom of the LMO and equilibrate with the melt at the respective pressure conditions. The depth of the LMO and its bottom pressure were updated after each crystallization step according to the volume of the crystallized cumulate. All the precipitated plagioclase was assumed to float to the surface and form the anorthositic crust.

At high pressure, the pMELTS algorithm produces garnet as a liquidus phase, which is inconsistent with fractional crystallization experiments (Elardo et al., 2011; Rapp & Draper, 2018). By suppressing garnet formation in the model, the bulk mineralogies of experimental studies (Charlier et al., 2018; Rapp & Draper, 2018) can be reproduced with deviations smaller than 3 vol%.

2.2. Thermochemical Convection

To simulate the dynamics of the overturn and the thermochemical evolution of the mantle, we used our finite-volume code Gaia (Hüttig et al., 2013) to solve the conservation equations of mass, linear momentum, and thermal energy under the Boussinesq approximation for a fluid with infinite Prandlt number heated from within by decaying heat sources and from below by the core (e.g., Laneuville et al., 2013; Tosi, Grott, et al.,2013). In addition, we used the particle-in-cell method as implemented in Gaia (Plesa et al., 2012) to solve a nondiffusive transport equation to treat the advection of chemical composition. In nondimensional form, the equations read respectively:

$$\nabla \cdot \boldsymbol{u} = 0, \tag{1}$$

$$-\nabla p + \nabla \left[\eta \left(\nabla \boldsymbol{u} + (\nabla \boldsymbol{u})^T\right)\right] = \left(Ra\, T - Ra_C\, C\right) \boldsymbol{e}_r, \tag{2}$$

$$\frac{\partial T}{\partial t} + \boldsymbol{u} \cdot \nabla T = \nabla^2 T + H \frac{Ra_Q}{Ra}, \tag{3}$$

$$\frac{\partial C}{\partial t} + \boldsymbol{u} \cdot \nabla C = 0, \tag{4}$$

where u is the velocity vector, p the dynamic pressure, η the viscosity, T the temperature, C the composition from which also the weighting function H is computed (see below), and e_r the unit radial vector. The nondimensional quantities Ra, Ra_C, and Ra_Q are the thermal Rayleigh number, the compositional Rayleigh number, and the Rayleigh number for internal heat sources, respectively, which are defined as follows:

$$Ra = \frac{\alpha \rho_\mathrm{m} g \Delta T D^3}{\eta_\mathrm{r} \kappa}, \tag{5}$$

$$Ra_C = \frac{\left(\rho_\mathrm{IBC} - \rho_\mathrm{cr}\right) g D^3}{\eta_\mathrm{r} \kappa}, \tag{6}$$

$$Ra_Q = \frac{\alpha \rho_\mathrm{m}^2 g Q D^5}{\eta_r \kappa k}, \tag{7}$$

where α is the thermal expansivity, ρ_m, ρ_IBC, and ρ_cr the density of the mantle, IBC, and crust, respectively, g is the gravitational acceleration, D the mantle thickness, η_r the reference viscosity (see equation (12) below), κ the thermal diffusivity, $\Delta T = T_\mathrm{c} - T_\mathrm{s}$ the initial temperature difference across the mantle (T_c is the initial CMB temperature), $Q = Q(t)$ is a time-dependent heat production rate, and k the thermal conductivity. With the exception of the viscosity (see equations (11) and (12) below), we kept all other parameters constant. Because of the limited pressure range of the lunar mantle (≈4–5 GPa) both the thermal conductivity and expansivity are expected to vary with depth by 10–20% at most (e.g., Tosi, Yuen, et al., 2013). Although

Table 1
Parameter Values Used in the Numerical Simulations

Symbol	Description	Value	Unit
R_p	lunar radius	1,740	km
R_c	core radius	390	km
D_{cr}	crust thickness	43	km
D_{IBC}	IBC thickness	36	km
D	mantle thickness	1,350	km
g	gravity acceleration	1.6	g/m^2
T_s	surface temperature	250	K
T_c	initial CMB temperature	2180	K
ΔT	temperature scale	1930	K
T_r	reference temperature	1600	K
α	thermal expansivity	3×10^{-5}	K^{-1}
κ	thermal diffusivity	10^{-6}	m^2/s
k	thermal conductivity	4.0	W·m^{-1}·K^{-1}
c_c	core heat capacity	840	J·K^{-1}·mol^{-1}
Q_{cr}	initial crust heat production rate	3.11×10^{-10}	W/kg
Q_{IBC}	initial IBC heat production rate	4.35×10^{-11}	W/kg
Q_m	initial mantle heat production rate	2.77×10^{-12}	W/kg
$\tau_{1/2}$	half-life	1.63	Gyr
ρ_{cr}	crust density	2,715	kg/m^3
ρ_{IBC}	IBC density	4,012	kg/m^3
ρ_m	mantle density	3,204	kg/m^3
ρ_c	core density	7,200	kg/m^3
η_r	reference viscosity	10^{18}–10^{21}	Pa s
E	activation energy	100–300	kJ/mol
V	activation volume	$0, 6 \times 10^{-6}$	m^{-3}·mol^{-1}
$\Delta\eta_{IBC}$	IBC to mantle viscosity ratio	0.1, 1	–

Note. All parameters were held fixed apart from the reference viscosity η_r, activation energy E, activation volume V, and IBC-mantle viscosity contrast $\Delta\eta_{IBC}$ that have been varied.

considering the depth dependence of these quantities can lead to some differences in the global long-term evolution of the interior (Zhao et al., 2016), the dynamics of the overturn on which we focus in this work is not going to be significantly affected. In contrast to the small variations of thermal expansivity and conductivity, the gravity acceleration decreases by nearly a factor of 3 from the surface ($g = 1.67$ m/s^2) to the CMB ($g = 0.6$ m/s^2) due to the small size of the core (e.g., Garcia et al., 2011). As we will show in section 3.2, the effects of radial gravity variation on the IBC overturn, which is largely controlled by the properties of the shallow mantle, are minor, and in most of the simulations we consider a constant gravity acceleration. Numerical values of the parameters that we used are reported in Table 1.

Nondimensional variables in equations (1)–(4) are obtained employing usual scaling factors. The length is scaled with the mantle thickness D; the time with the diffusion time scale D^2/κ; the velocity with κ/D; the pressure with $\eta_r\kappa/D^2$; the temperature with the temperature scale ΔT.

As we will show in section 3.1, for our dynamic simulations we simplified the crystallization sequence of the LMO calculated with alphaMELTS by considering three main materials, namely the crust, IBC, and mantle. We defined the composition field C as

$$C = \frac{\rho_i - \rho_{cr}}{\rho_{IBC} - \rho_{cr}}, \tag{8}$$

where ρ_i is the dimensional density of crust, IBC, or mantle. Upon solving the momentum equation (2), the compositional buoyancy term is obtained by locally averaging the field C (which is defined on particles)

around every grid point (Plesa et al., 2012). The weighting function H is defined simply by scaling the heat production rate of each of the three materials with that of the IBC, that is,

$$H = Q_i / Q_{\mathrm{IBC}}, \tag{9}$$

where Q_i is the heat production rate of the crust, IBC, or mantle, whose values, like those of the density, are reported in Table 1. The dimensional heat production rate appearing in the Rayleigh number for internal heating (equation (7)) decreases exponentially with time according to the expression:

$$Q = Q_{\mathrm{IBC}} \exp\left(-\ln(2) t / \tau_{1/2}\right), \tag{10}$$

where $\tau_{1/2}$ is a lumped half life that accounts for the decay of the three long-lived radiogenic isotopes of U, Th, and K. Note, however, that within the relatively short time scale over which we run our simulations (200 Myr), radiogenic decay plays a nearly negligible role for the mobilization of the IBC layer.

We considered a linear mantle rheology with a viscosity that can also depend on composition. Ilmenite is a rheologically weak component in the ilmenite-olivine aggregate (Dygert et al., 2016). In the presence of some amount of ilmenite, mantle materials may have a lower viscosity with respect to the pure end-member. In order to account for this possibility, we calculate the viscosity as follows:

$$\eta = \left(\frac{1 - \phi_{\mathrm{IBC}}}{\eta_{\mathrm{m}}} + \frac{\phi_{\mathrm{IBC}}}{\Delta\eta_{\mathrm{IBC}} \eta_{\mathrm{m}}} \right)^{-1}, \tag{11}$$

where ϕ_{IBC} is the volume fraction of IBC, η_{m} the mantle viscosity (see below), and $\Delta\eta_{\mathrm{IBC}}$ a prefactor that controls the viscosity contrast between IBC and lunar mantle. In determining equation (11), we adopted the isostress mixing model, the so-called Reuss model, to blend the rheology of ilmenite and lunar mantle. This model can provide a good approximation of the rheology of ilmenite-contaminated mantle materials at the typical strain of mantle convection (Dygert et al., 2016; Jordan, 1987). For the mantle, we assumed a strongly temperature-dependent viscosity based on the Arrhenius law for diffusion creep, whose dimensional form reads as follows:

$$\eta_{\mathrm{m}} = \eta_{\mathrm{r}} \exp\left(\frac{E}{RT} - \frac{E}{RT_{\mathrm{r}}} \right), \tag{12}$$

where E is the activation energy, R the gas constant, and η_{r} the reference viscosity at reference temperature T_{r}. In equation (12), we neglected the contribution pV (i.e., pressure times activation volume) to the activation enthalpy because of the small pressure range of the lunar mantle (≈4 GPa (e.g., Wieczorek et al., 2006). For a typical value of the activation volume of $6 \cdot 10^{-6}$ m^3/mol (e.g., Hirth & Kohlstedt, 2003), pV contributes 24 kJ/mol to the activation enthalpy, which results only in a slight increase of the viscosity with pressure (about a factor 4 at 4 GPa and 2000 K). In section 3.2 we demonstrate that this contribution is indeed negligible. In order to limit the extremely high viscosity implied by the Arrhenius law (12) at low temperatures, we imposed a fixed maximum viscosity contrast $\Delta\eta_{\mathrm{max}}$ of 10^{10}, large enough for all our simulations to be well in the stagnant lid regime (e.g., Guerrero et al., 2018). Specifically, the minimum viscosity (η_{min}) obtained from equation (11) is free to vary according to temperature and composition, while the maximum viscosity is recalculated at each time step as $\eta_{\mathrm{max}} = \eta_{\mathrm{min}} \Delta\eta_{\mathrm{max}}$. This ensures that the viscosities obtained in the region relevant for the overturn are not modified by artificial cuts. All parameter values used in the simulations are reported in Table 1.

The conservation equations (1)–(4) were solved in a half-cylindrical domain (i.e., with angular coordinate from 0 to π) meshed with a structured grid where each shell of the domain contains the same number of computational nodes. The grid has a uniform radial resolution of 4.5 km and a lateral resolution varying from approximately 3 km at the CMB to 14 km at the surface. The high resolution allows us to properly resolve the dynamics of the IBC whose initial thickness, as we will show in section 3.1, is just 36 km, and to deal with very low viscosities that cause convection to be characterized by small spatial scales. All domain boundaries were assumed to be free slip and impermeable. Energy conservation was solved using isothermal surface and CMB, and insulating sidewalls. Since here we focus only on the overturn phase and early dynamics of the solid-Moon evolution, we updated the temperature of the CMB using a simple core-cooling boundary condition:

$$\rho_{\mathrm{c}} c_{\mathrm{c}} V_{\mathrm{c}} \frac{\partial T_{\mathrm{c}}}{\partial t} = -q_{\mathrm{c}} A_{\mathrm{c}}, \tag{13}$$

where ρ_c is the core density, c_c the core heat capacity, V_c the core volume, T_c the CMB temperature, q_c the laterally averaged heat flux at the base of the mantle calculated at each time step according to the evolving temperature gradient at the CMB, and A_c the area of the CMB. In equation (13) we neglect the release of latent heat and the change of gravitational potential energy caused by inner core growth due to their secondary role in controlling the CMB heat flux during the first 500 Myr of lunar evolution (Laneuville et al., 2014). Furthermore, it is unlikely for the inner core to start growing before ≈200 Myr (Laneuville et al., 2014), the time interval over which we run our simulations.

The initial profiles of temperature and composition are obtained from modeling of the crystallization sequence of the LMO (see Figure 4), which is presented in section 3.1. Convection was initiated by imposing a small random perturbation with an amplitude of 1% of ΔT on the initial temperature field.

2.3. Tracking the Cumulate Overturn

Choosing to perform our simulations in a 2-D cylindrical geometry allows us to reach a high resolution that would be difficult to achieve in a fully spherical geometry. Such a high resolution is necessary to deal both with the overturn of the thin IBC layer (36 km as shown in section 3.1) and with very low viscosities that cause convection to be small scale (see section 2.4). Although the use of a cylindrical geometry does not affect the rheological conditions for the overturn, it influences the final thickness of the overturned IBC—a parameter adopted to track the overturn of IBC in previous investigations—once these accumulate above the core. Assuming that all the overturned IBC finally deposit onto the bottom of lunar mantle, Figure 1a shows the thickness of the overturned IBC above the CMB in 2-D-cylinderical and spherical geometry as a function of $\Delta D_{IBC}/D_{IBC}$, where ΔD_{IBC} is the thickness of mobilized IBC and D_{IBC} is the initial thickness of the crystallized IBC layer (36 km in this work). Here $\Delta D_{IBC}/D_{IBC} = 0$ if IBC do not overturn and 1 if they overturn completely. As shown in the figure, such thickness tends to be strongly underestimated when using a cylindrical geometry. We also note that the thickness of overturned IBC estimated here is just representative of an ideal condition. As we will show below (see Figures 6 and 7), the amount and, correspondingly, the thickness of overturned IBC can also be affected by mixing of these cumulates with the underlying mantle material.

To avoid the influence of the geometry upon tracking the mobility of IBC, we simply tracked the evolution of the volumetric fraction of the overturned IBC (i.e., mobilized from its initial position in the shallow mantle) as follows:

$$\psi_{IBC} = \frac{V_{IBC} - V'_{IBC}}{V_{IBC}} \times 100\%, \tag{14}$$

where V_{IBC} is the total volume of IBC and V'_{IBC} is the volume of IBC, which does not participate in the overturn and remains locked in the stagnant lid. In Figure 1b, we plot the ratio between the ψ_{IBC} calculated for a 2-D cylinder and a 3-D sphere as a function of $\Delta D_{IBC}/D_{IBC}$. The 2-D cylinder affects ψ_{IBC} by ≈1% at most, indicating that this quantity is insensitive to the domain geometry.

As the thickness of overturned IBC above the CMB is sensitive to the domain geometry, it is not appropriate to employ a 2-D-cylindrical geometry to investigate the postoverturn thermochemical evolution of the Moon. Once IBC accumulate above the CMB, their convective instability, which might develop as a long-wavelength structure, also depends on the domain geometry and on the thickness of the overturned layer (e.g., Zhang et al., 2013b). Because of this limitation, here we restrict our analysis to the overturn phase.

2.4. Model Parameters

We held all model parameters fixed except for the reference viscosity (η_r), activation energy (E), and viscosity contrast between IBC and mantle ($\Delta\eta_{IBC}$), which are the free parameters of our simulations (see equations (11) and (12)). We varied the reference viscosity η_r at 1600 K from 10^{18} to 10^{21} Pa s. The value of 10^{21} Pa s approaches the viscosity of dry peridotite (e.g., Hirth & Kohlstedt, 2003). The lower limit of 10^{18} Pa s is characteristic of a weak rheology, representative of a hydrated mantle, with a possible role for deformation via dislocation creep. Additionally, we tested the effects of the pressure dependence of the viscosity by running two selected simulations accounting for an activation volume of 6 cm^3/mol (see section 3.2 and Figure 5).

Recent investigations on lunar picritic glasses suggest that the bulk Moon is significantly more water-rich than previously thought. By taking into account volatile degassing during magma eruptions, the water content of primitive lunar magmas was estimated to be of the order of hundreds of parts per million (Hauri et al.,

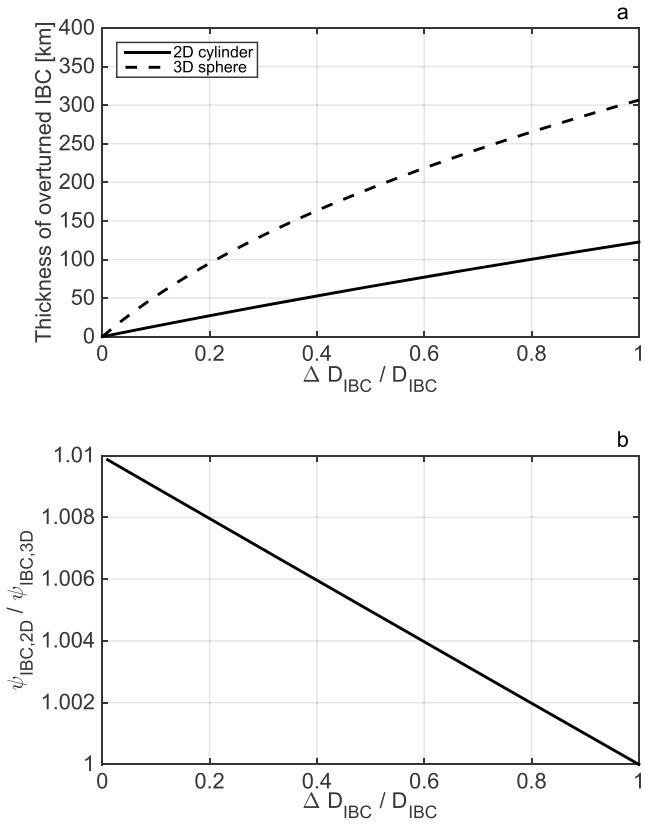

Figure 1. (a) Thickness of overturned ilmenite-bearing cumulates (IBC) and (b) ratio between ψ_{IBC} for a 2-D cylinder and a 3-D sphere as functions of $\Delta D_{IBC}/D_{IBC}$, where ΔD_{IBC} is the thickness of mobilized IBC.

2015; Saal et al., 2008). Based on free oscillations data and lunar electromagnetic sounding, Karato (2013) also suggested that the bulk Moon could contain as much water as the Earth's asthenosphere (≈100 ppm). Assuming an activation energy for diffusion creep of 300 kJ/mol, a water concentration of approximately 600 ppm would be required to achieve a viscosity of 10^{18} Pa s at 1600 K in absence of melt (Hirth & Kohlstedt, 2003). Considering, for example, a trapped melt fraction of 2% or 5%, the same viscosity would be obtained with water concentrations of ≈345 ppm or ≈140 ppm, respectively.

Alternatively, deformation via power law dislocation creep (not explicitly considered in this work) could also contribute to reduce the reference viscosity to such a low level. In Figure 2, we plot the viscosity as a function of temperature associated with pure diffusion creep and with a hybrid rheology, which couples dislocation and diffusion creep. For this plot, we used flow laws for diffusion and dislocation creep of olivine from Hirth and Kohlstedt (2003) together with the isostress mixing model (Jordan, 1987), and considered reference viscosities of 10^{21} Pa (Figure 2a), 10^{20} Pa (Figure 2b), and 10^{19} Pa (Figure 2c) corresponding to grain sizes of 12.1, 5.6, and 2.6 mm, respectively.

Besides the reference viscosity, we varied the activation energy between 100 and 300 kJ/mol. Estimates of the activation energy for the deformation of dry olivine in the diffusion creep regime range from 300 (Karato & Wu, 1993) to 375 kJ/mol (Hirth & Kohlstedt, 2003). Wet diffusion creep in olivine is typically associated with slightly lower activation energies, between 240 (Karato & Wu, 1993) and 335 kJ/mol (Hirth & Kohlstedt, 2003). Christensen (1984) suggested that the thermal effects of power law creep can be reproduced by a diffusion creep rheology with an effective activation energy reduced by a factor between 2 and 3. Values of the activation energy near the lower end of the investigated range (100 kJ/mol) reflect this idea. Furthermore, as shown in Figure 2, the viscosity of a mantle deforming with a composite rheology would also exhibit a weaker temperature dependence, which is indicative of a reduced effective activation energy.

As a rheologically weak component within the ilmenite-olivine mixture, the presence of ilmenite can also reduce the viscosity of ilmenite-bearing materials. Figure 3 shows the viscosity of IBC as a function of

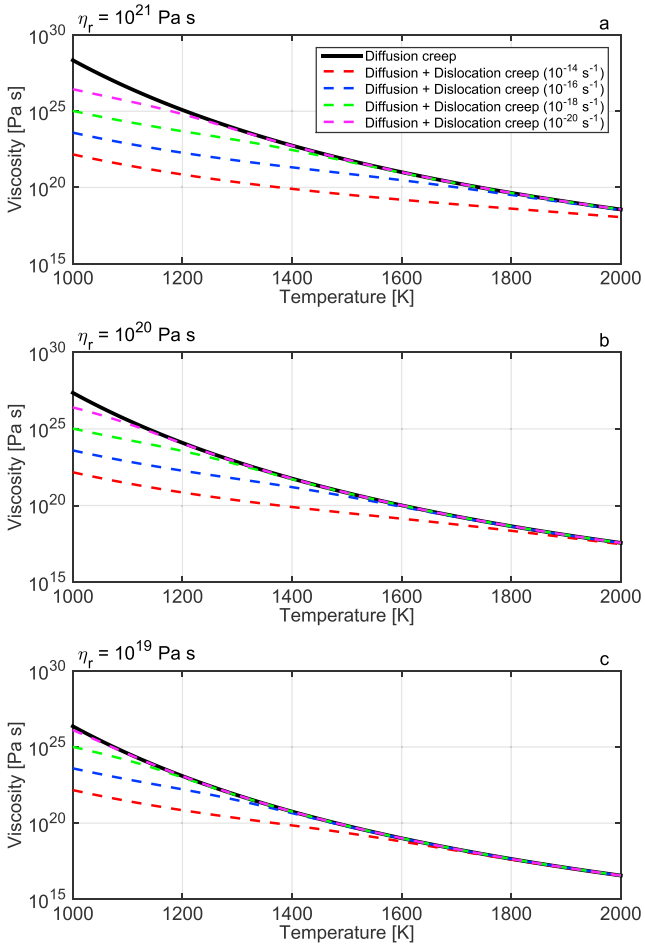

Figure 2. Viscosity of olivine deforming via diffusion creep (black lines) and via a hybrid rheology coupling diffusion and dislocation creep based on different strain rates (colored lines) for reference viscosities at 1600 K of 10^{21} Pa s (a), 10^{20} Pa s (b), and 10^{19} Pa s (c), corresponding to grain sizes of 12, 5.6, and 2.6 mm, respectively. Rheological parameters and flow laws are from Hirth and Kohlstedt (2003).

temperature obtained with an ilmenite content of 6.7 vol.% (as predicted by our crystallization model) and different strain rates based on the experimental data of Dygert et al. (2016) and the isostress mixing model to blend the rheology of ilmenite and peridotite. The viscosity of IBC shows a weaker temperature dependence, indicative of a lower effective activation energy and, depending on the strain rate, can be up to few orders of magnitude lower than the diffusion creep viscosity of olivine.

Overall, at a temperature of ≈1400 K where IBC crystallize (see section 3.1), the viscosity of diffusion creep (black lines in Figures 2 and 3) is ≈10^{23}, ≈10^{22}, and ≈10^{21} Pa s for reference viscosities of 10^{21}, 10^{20}, and 10^{19} Pa s, respectively. If diffusion creep is coupled with olivine dislocation creep (as in Figure 2) or with ilmenite dislocation creep (as in Figure 3), the resulting viscosity is significantly reduced. For example, for a relatively large strain rate of 10^{-14} s^{-1}, at 1400 K, such reduction is of about 3, 2, and 1 orders of magnitude when assuming reference viscosities of 10^{21}, 10^{20}, and 10^{19} Pa s, respectively (compare red dashed and black lines in Figures 2 and 3).

Here, we just varied the prefactor $\Delta\eta_{\mathrm{IBC}}$ associated with the rheological contrast between mantle and IBC between 0.1 (corresponding to a weak IBC) and 1 (corresponding to no compositional viscosity contrast). From a numerical standpoint, carrying out simulations at very low reference viscosities and high activation energies such as those considered in this work, is very challenging. In some cases, upon considering the additional viscosity reduction associated with the IBC, we encountered convergence problems in our numerical solution scheme that prevented us from carrying out simulations with viscosity contrasts $\Delta\eta_{\mathrm{IBC}}$ significantly smaller than 0.1.

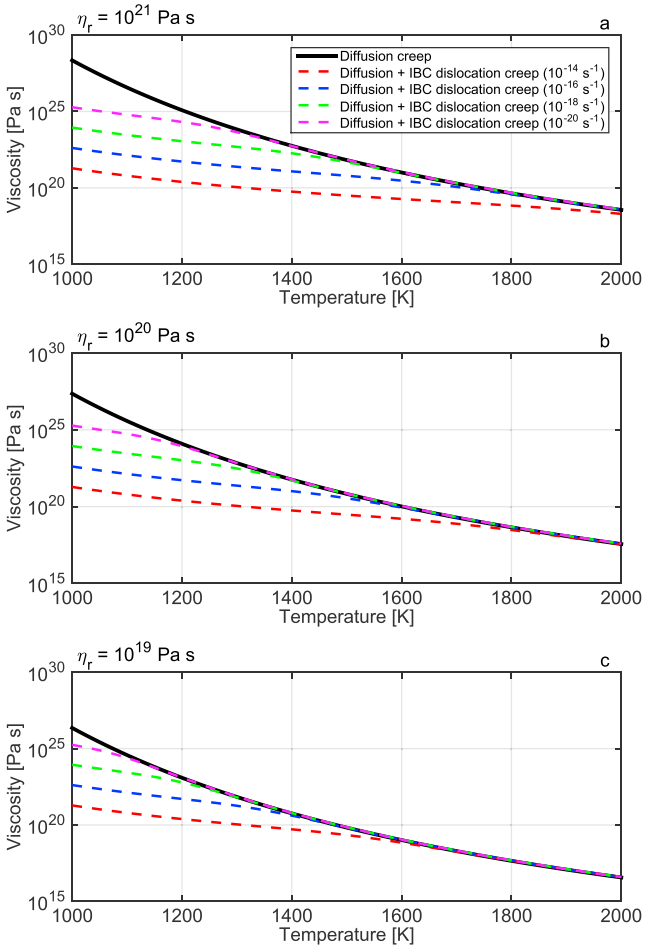

Figure 3. Viscosity of olivine deforming via diffusion creep (black lines) and viscosity of ilmenite-bearing cumulates based on different strain rates (colored lines) for reference viscosities of 10^{21} Pa s (a), 10^{20} Pa s (b) and 10^{19} Pa s (c), corresponding to grain sizes of 12, 5.6, and 2.6 mm, respectively. The ilmenite content of IBC is 6.7 vol.%. The rheological parameters of ilmenite were taken from Dygert et al. (2016).

3. Results

3.1. Crystallization Sequence and Initial Conditions

Using the crystallization model described in section 2.1, we calculated initial profiles of density, temperature, and heat production rate (Figure 4). The resulting thickness of the plagioclase crust is 43 km, in good agreement with recent estimates based on the analysis of Gravity Recovery and Interior Laboratory (GRAIL) data (Wieczorek et al., 2013). We identified the IBC layer with the depth range over which TiO_2-rich phases (Ti-spinel, ilmenite and titanite) crystallize. The thickness of this layer is 36 km, also in good agreement with previous studies (e.g., Hess & Parmentier, 1995). The average ilmenite content of IBC is ≈6.7 vol.%. As mentioned in section 2.1, this thickness is obtained by maximizing the Ti content and represents thus an upper limit. Using minimum estimates of Ti content leads to an IBC thickness of ≈33 km. Lower values can be obtained by reducing the initial magma ocean thickness. For a 1,000-km-thick magma ocean with a high Ti content, the IBC layer has a thickness of ≈26 km. The bulk composition also plays a role. At the lower end of possible thicknesses, we obtained 6.5 km when using the bulk composition of Longhi (2003) together with a 1,000-km-thick magma ocean and the lowest possible Ti-content. The mantle beneath the IBC is largely composed of olivine and pyroxene cumulates.

The abrupt jumps in the density distribution around a radius of 1,600 km and within the IBC (Figure 4a) are due to oscillatory changes of the liquidus phase that occur where several phases are stable close to the liquidus temperature and thus small changes in the liquid composition by fractional crystallization can cause a change of the liquidus phase.

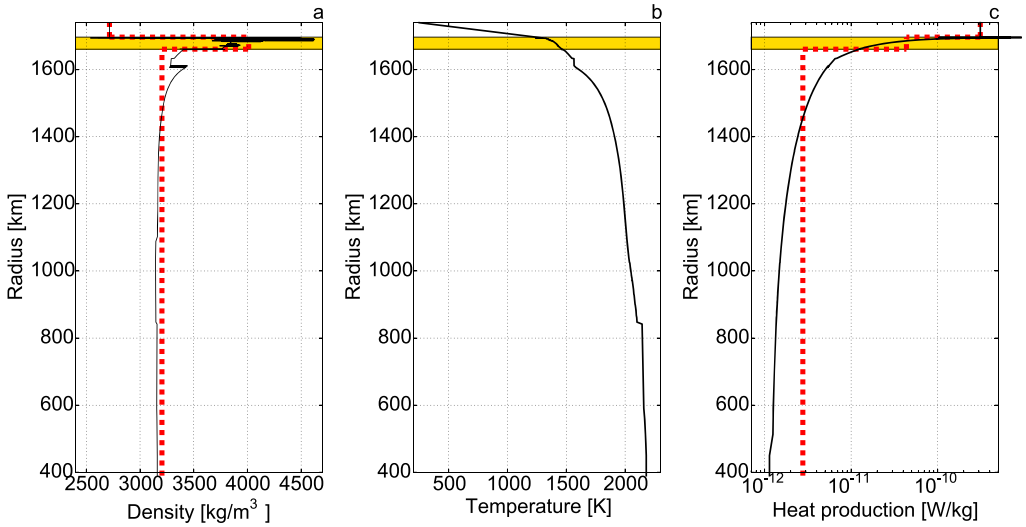

Figure 4. Profiles of density (a), temperature (b), and heat production rate (c) resulting from the crystallization of the lunar magma ocean in a spherical shell. Black lines indicate the profiles calculated with alphaMELTS, while dashed red lines indicate the simplified three-layer model used in the simulations. The yellow bar indicates the initial location of the IBC.

As discussed above, for our dynamic simulations, we simplified the profiles obtained with alphaMELTS by introducing a three-layer configuration consisting of mantle, IBC, and crust to which we assigned volume-averaged values of density and heat production rate (red dashed lines in Figures 4a and 4c). For the initial temperature distribution, we used the profile shown in Figure 4b, which we calculated assuming that each cumulate layer retains its crystallization temperature over the time scale of LMO solidification. The initial temperature profile across the plagioclase crust was simply assumed to be linear with a surface temperature of 250 K.

A KREEP layer with a thickness of about 1 km crystallizes beneath the plagioclase crust and is considered part of it upon averaging its density and heat production. The high heat production of the crust (Figure 4c) is also due to the heat sources contained in such a layer.

3.2. Overturn of IBC

Using the radial distributions of composition, temperature, and heat production rate of Figure 4 as initial conditions, we ran our dynamical simulations keeping track of the fate of the IBC layer. For different combinations of reference viscosities between 10^{18} and 10^{21} Pa s and activation energies between 100 and 300 kJ/mol, Figure 5a shows initial viscosity profiles assuming no rheological contrast between mantle and IBC (i.e., $\Delta\eta_{\mathrm{IBC}} = 1$ in equation (11)). Upon considering a weak IBC layer, the viscosity profiles shown in Figure 5a are reduced by 1 order of magnitude within the IBC layer (i.e., $\Delta\eta_{\mathrm{IBC}} = 0.1$). These profiles are calculated along the crystallization temperature of Figure 4b and plotted down to a radius of 1,600 km, close to the depth at which the reference temperature of 1600 K is attained. On the one hand, the higher is the activation energy, the stronger is the temperature dependence of the viscosity and, as a consequence, the more rapidly the stagnant lid will grow. On the other hand, a higher reference viscosity results in a less vigorous convection and a slower development of the overturn, leaving more time for the stagnant lid to grow thick enough to prevent IBC from being mobilized.

In Figure 5b, assuming first $\Delta\eta_{\mathrm{IBC}} = 1$, we plot the volumetric fraction of overturned IBC as a function of time for combinations of activation energies and reference viscosities for which at least part of the IBC layer can be mobilized. For a reference viscosity of 10^{21} Pa s (not shown in the figure), IBC do not sink, independent of the activation energy. For a reference viscosity of 10^{20} Pa s, they are trapped in the stagnant lid if the activation energy is set to 300 kJ/mol, which is similar to the results of Elkins-Tanton et al. (2002). By decreasing the activation energy to 200 and 100 kJ/mol, the volumetric fraction of overturned IBC increases to 14% and 85%, respectively. Independent of the activation energy, more than 95% IBC can eventually sink for reference viscosities of 10^{18} and 10^{19} Pa s, which indicates the central role of this parameter in controlling the overturn. In Figure 5b we also show two additional simulations with an activation energy of 100 kJ/mol

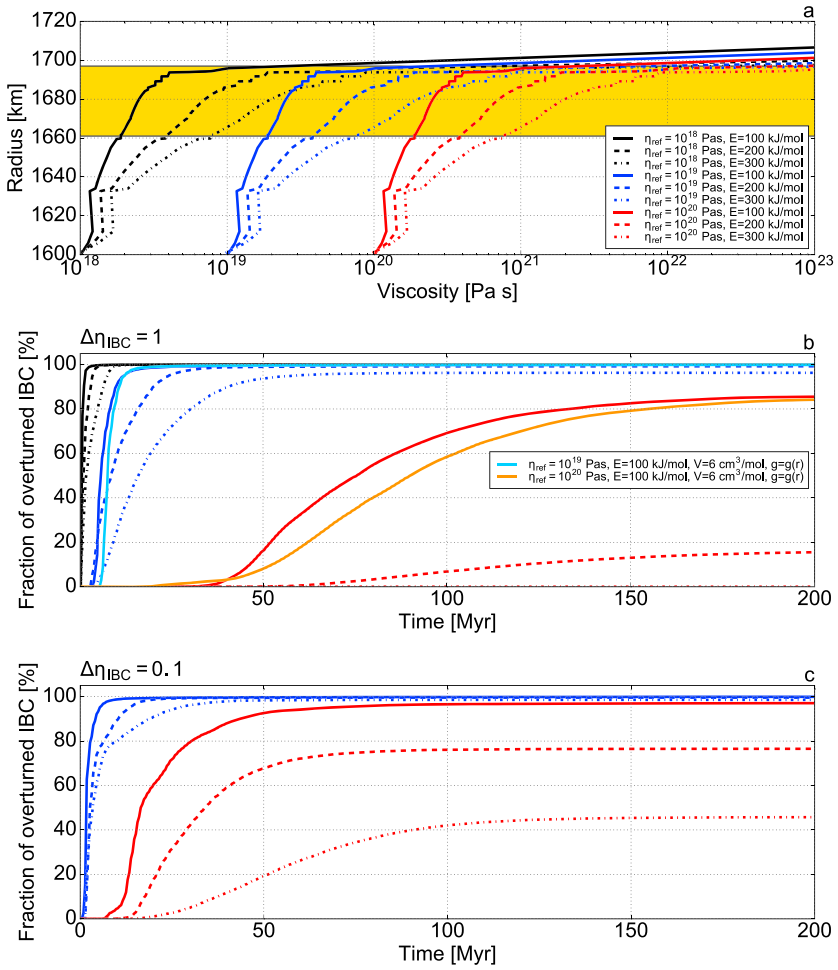

Figure 5. (a) Initial viscosity profiles calculated along the temperature profile of Figure 4b for different combinations of reference viscosity and activation energy assuming no rheological contrast between mantle and IBC. The yellow bar indicates the initial location of the IBC layer. (b) Volume-fraction of overturned IBC as a function of time for the above cases and two additional cases where the depth dependence of both the viscosity and of the gravity acceleration are taken into account. Low activation energies and reference viscosities promote early mobilization and increase the fraction of overturned IBC. (c) Volume-fraction of overturned IBC as a function of time for reference viscosities of 10^{19} and 10^{20} Pa s and assuming IBC to have a viscosity lower than the viscosity of the lunar mantle by 1 order of magnitude. For the highest reference viscosity that we tested ($\eta_r = 10^{21}$ Pa s), no IBC overturn was observed, independent of the activation energy and of the viscosity reduction of IBC.

and reference viscosities of 10^{19} Pa s (light blue) and 10^{20} Pa s (orange) in which we took into account the depth dependence of both the gravitational acceleration and the viscosity. The strong similarity with the time series of the overturned IBC fraction where these two features are neglected (compare solid blue and red lines) indicates that the IBC mobilization is largely controlled by the thermomechanical properties of the shallow mantle.

The overturn of IBC is also facilitated by decreasing the viscosity of the IBC layer itself. In Figure 5c, we plot the volumetric fraction of overturned IBC as a function of time for reference viscosities of 10^{19} and 10^{20} Pa s taking into account a reduction of 1 order of magnitude of the IBC viscosity ($\Delta\eta_{IBC} = 0.1$). With a reference viscosity of 10^{19} Pa s, a weak IBC fully overturns, independent of the activation energy. With a reference viscosity of 10^{20} Pa s, the volumetric fraction of overturned IBC is systematically higher than in the previous set of simulations employing $\Delta\eta_{IBC} = 1$: 96%, 76%, and 45% for activation energies of 100, 200, and 300 kJ/mol, respectively. Again, for $\eta_{ref} = 10^{21}$ Pa s, IBC overturn does not take place, even for the lowest activation energy considered.

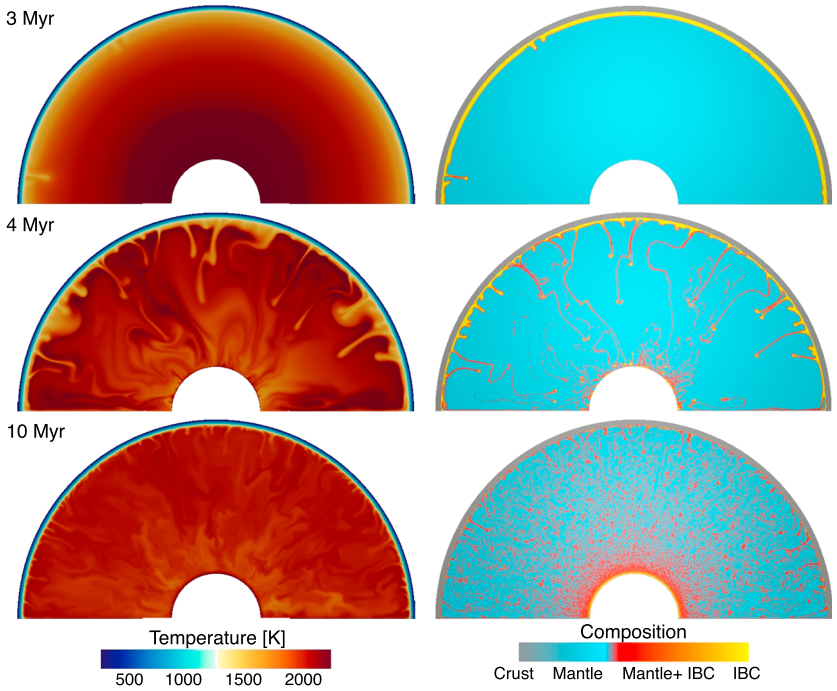

Figure 6. Snapshots of temperature (left column) and composition (right column) for a simulation with $\eta_r = 10^{19}$ Pa s and $E = 100$ kJ/mol after 3, 4, and 10 Myr. In the composition field, gray indicates crust material, light blue, mantle material, yellow, IBC, and red, IBC mixed with mantle material.

Figures 6 and 7 show various snapshots of the temperature and composition fields that illustrate the dynamics of the overturn for two cases with $\Delta\eta_{IBC} = 1$, $\eta_r = 10^{19}$, and either $E = 100$ kJ/mol (Figure 6) or $E = 300$ kJ/mol (Figure 7). In the first case, the overturn starts with multiple small-scale diapirs at the base of the IBC layer (Figure 6, top row). These sink rapidly while mixing with mantle material (Figure 6, middle row) and eventually accumulate above the CMB (Figure 6, bottom row). The use of a half cylinder plays here a minor but visible role in forcing a radial flow along the two sidewalls. In the second case, the high activation energy renders the IBC region stiffer. Because of the strong temperature dependence of the viscosity, thermal convection in the deep mantle starts before the onset of the compositional instability (Figure 7, top row), and when IBC begin to sink, thermal convection is already well developed (Figure 7, middle row). The relatively high viscosity of the uppermost mantle also causes IBC to drip significantly more slowly than in the previous case where a lower activation energy is used. After 10 Myr, while the overturn is completed when assuming $E = 100$ kJ/mol, most of the IBC still have to sink when assuming $E = 300$ kJ/mol (compare bottom rows of Figures 6 and 7). We observed the same behavior even when we accounted for a viscosity contrast of 1 order of magnitude between mantle and IBC (i.e., $\Delta\eta_{IBC} = 0.1$).

4. Rayleigh-Taylor Instability Analysis

To obtain a better insight into our modeling results, we use here the theory of Rayleigh-Taylor instability to analyze the overturn of IBC (Scheinberg et al., 2018). A growing Rayleigh-Taylor instability can be described using the relation:

$$w = w_0 \exp\left(\frac{t}{t_{onset}}\right) \tag{15}$$

where w is the dimensional vertical velocity, w_0 its initial amplitude, and t_{onset} is the so-called (dimensional) onset time. With free-slip boundaries, the onset time of the overturn at the dominant wavelength, that is, the wavelength characterized by the most rapid growth rate of vertical velocity, can be expressed as (Hess & Parmentier, 1995; Whitehead, 1988)

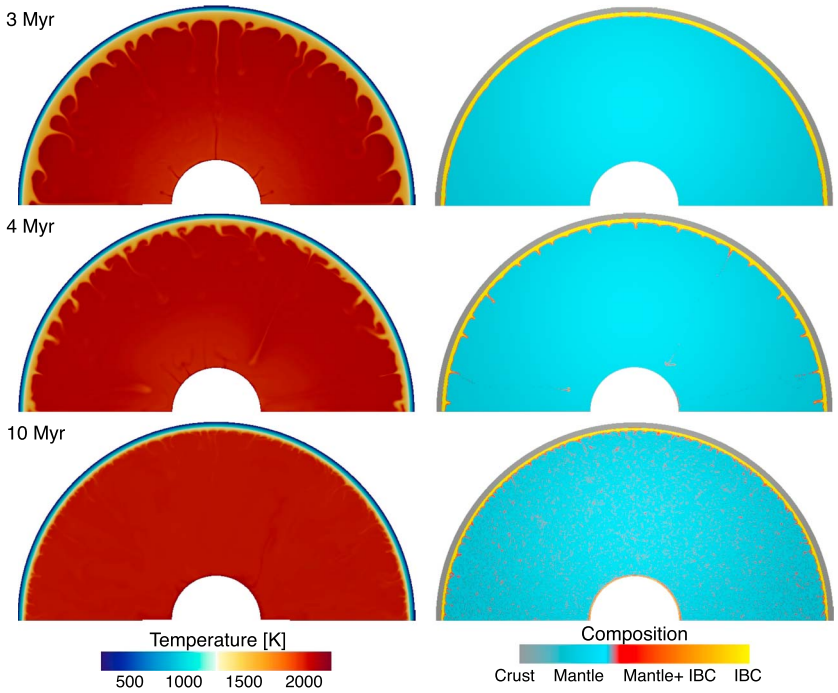

Figure 7. As in Figure 6 but assuming $\eta_r = 10^{19}$ Pa s and $E = 300$ kJ/mol.

$$t_{onset} = \frac{6.5\eta_m^{2/3}\eta_{IBC}^{1/3}}{(\rho_{IBC} - \rho_m)\, g_{IBC} D_{IBC}}, \tag{16}$$

where η_m is mantle viscosity, η_{IBC} the IBC viscosity, ρ_m and ρ_{IBC} the corresponding densities, g_{IBC} the gravitational acceleration at the depth of the IBC layer, and D_{IBC} the IBC thickness.

The viscosities η_m and η_{IBC} depend on the mantle temperature. Before the onset of the overturn, the heat transfer in the lunar mantle is controlled primarily by conduction. Therefore, we modeled the evolution of the mantle temperature before the overturn by solving a 1-D heat conduction equation:

$$\frac{\partial T}{\partial t} = \kappa \Delta^2 T + \frac{Q}{\rho c_p}. \tag{17}$$

where T is now the dimensional temperature, t the dimensional time, and Q the dimensional heat production rate. Here we used the temperature and heat production rate profiles of Figure 4 as initial conditions. Since we focused on the temperature evolution before the overturn phase, the heat sources were assumed to be fixed in space, but to decay with time. To be consistent with equation (16), we solved equation (17) in a Cartesian geometry.

Figure 8 shows temperature profiles at different times obtained from equation (17). The temperature across the IBC layer decreases with time. As a consequence, the IBC viscosity also increases and so does the onset time according to equation (16). The overturn of IBC cannot take place unless the onset time is shorter than the actual time that has elapsed, that is, $t_{onset} < t$. Otherwise, the viscosity of the IBC layer becomes too large to allow the vertical velocity to increase sufficiently with the consequence that the IBC will remain trapped in the growing stagnant lid.

We also note that equation (16) is derived by assuming the mantle and IBC viscosity to be constant. However, a depth-dependent temperature profile also leads to a depth-dependent viscosity profile. Therefore, to employ equation (16), we set η_m to the viscosity calculated at the IBC-mantle interface and η_{IBC} to the volumetrically averaged viscosity of the IBC layer. Both η_m and η_{IBC} are functions of temperature and hence of time.

Figure 9 shows the estimated onset time as a function of the actual simulation time for all combinations of activation energy and reference viscosity that we tested. In Figure 9a, corresponding to $\eta_r = 10^{21}$ Pa s, none

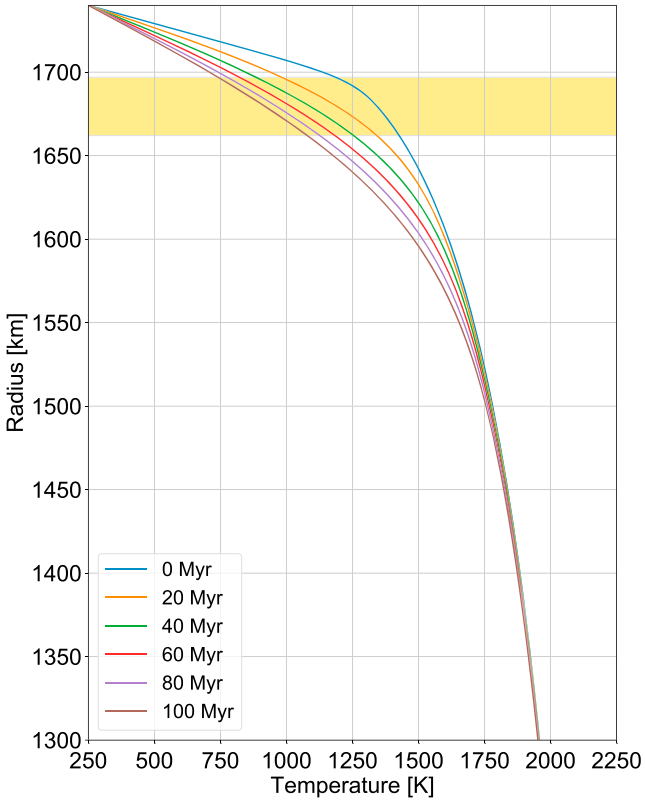

Figure 8. Temperature profiles at different times before the overturn phase obtained by solving equation (17). The yellow bar indicates the position of the ilmenite-bearing cumulates layer.

of the three curves, which correspond to different activation energies, intersects the dashed line that indicates the time elapsed, t, equals t_{onset}. Therefore, the overturn cannot take place for this reference viscosity, independent of the activation energy. Figure 9b ($\eta_{\mathrm{r}} = 10^{20}$ Pa s) shows that the overturn can take place for $E = 100$ kJ/mol, but it cannot for $E = 300$ kJ/mol and is marginally possible for $E = 200$ kJ/mol. The latter case is consistent with the overturn of a limited amount of IBC as predicted by our dynamic models (see red dashed line in Figure 5b). In Figures 9c and 9d ($\eta_{\mathrm{r}} = 10^{19}$ Pa s and $\eta_{\mathrm{r}} = 10^{18}$ Pa s), all curves intersect with the dashed line, which implies that the overturn of IBC is always possible. These results are consistent with, and explain the physical controls on the overturns in the dynamic simulations shown in Figure 5b.

We note that the intersection region for which $t_{\mathrm{onset}} < t$ just specifies the regime in which the overturn of IBC is possible, but does not indicate when the overturn is going to be significant. For example, the red solid curve in Figure 9b intersects the dashed line at ≈1 Myr, but the increase of ψ_{IBC} becomes significant at ≈40 Myr when using the same combination of reference viscosity and activation energy (see Figure 5b). In fact, the fraction of mobilized IBC can be related to the amplitude of the Rayleigh-Taylor instability as follows:

$$\psi_{\mathrm{IBC}} \approx \frac{w_0}{D_{\mathrm{IBC}}} \int_0^t \exp\left(\frac{t'}{t_{\mathrm{onset}}}\right) \mathrm{d}t' . \tag{18}$$

We thus obtain

$$\frac{\mathrm{d}\psi_{\mathrm{IBC}}}{\mathrm{d}t} \approx \frac{w_0}{D_{\mathrm{IBC}}} \exp\left(\frac{t}{t_{\mathrm{onset}}}\right) . \tag{19}$$

Equaion (19) implies that the growth of ψ_{IBC} not only depends on the onset time but also on the initial vertical velocity. At $t = t_{\mathrm{onset}}$, the growth rate of ψ_{IBC} is just $\approx 2.718 w_0/D_{\mathrm{IBC}}$. As an initial vertical velocity perturbation, the value of w_0 is far smaller than the value of IBC thickness. It is therefore necessary to expect that a significant overturn develops later than the theoretical onset time. Since the IBC thickness is

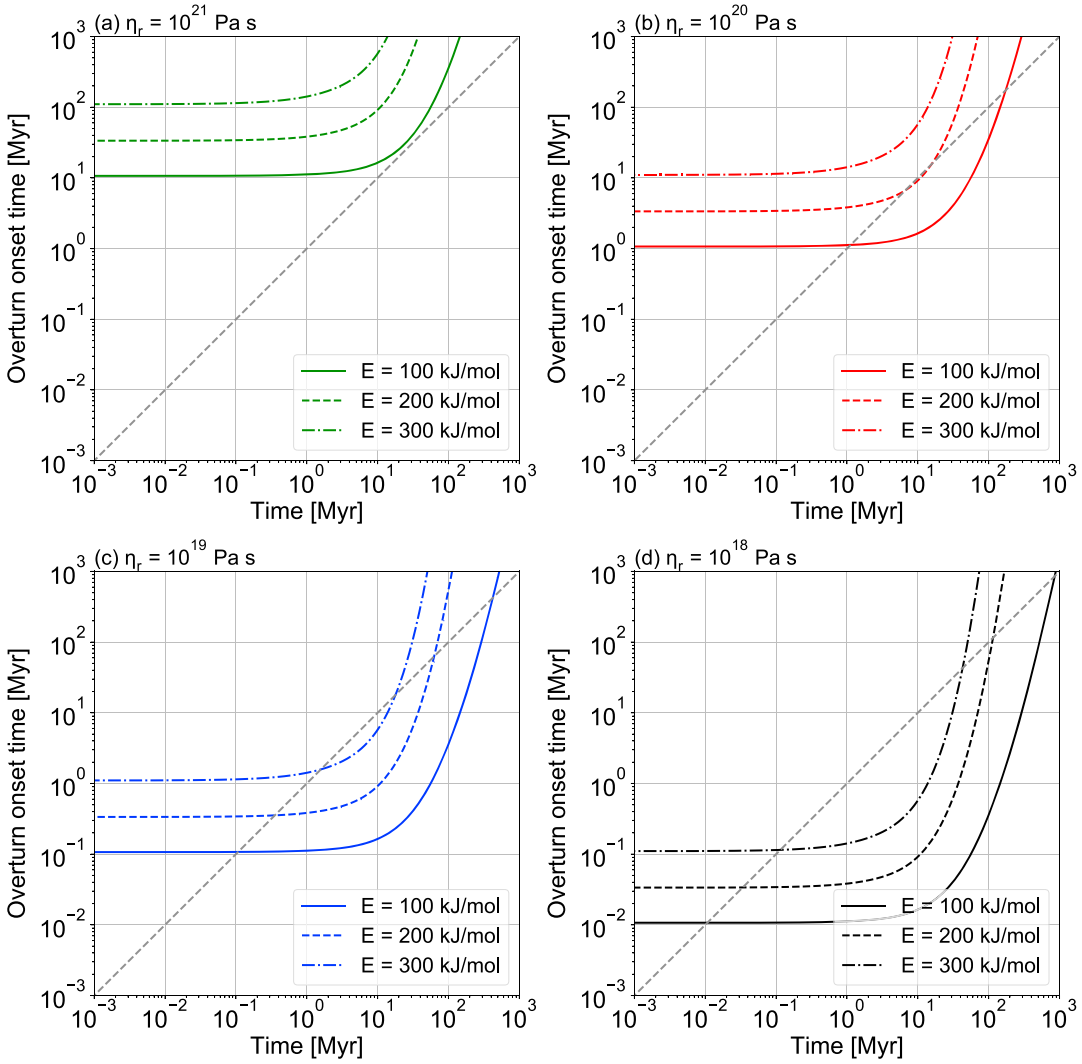

Figure 9. Onset time of the overturn based on a model of Rayleigh-Taylor instability for all combinations of activation energy (E) and reference viscosity (η_r). The time evolution is obtained from equation (16) by computing the ilmenite-bearing cumulates and mantle viscosity according to the temperature calculated with a conductive cooling model (equation (17)). Mobilization of the ilmenite-bearing cumulates layer is possible if the onset time is smaller than the actual time.

much smaller than the thickness of the lunar mantle, equations (18) and (19) are also applicable to cases in spherical and cylindrical geometry.

5. Discussion

As previously recognized by Elkins-Tanton et al. (2002), the rheology of the lunar mantle determines whether the overturn of IBC can take place or not. Similar to their results, we found that the overturn cannot take place with the typical reference viscosity and activation energy of dry olivine. However, it can be facilitated by reducing the reference viscosity, or the activation energy, or the IBC viscosity.

An important factor that can contribute to reducing the reference viscosity, as we discussed earlier, is the presence of water. With a bulk water content of hundreds of parts per million, the reference viscosity can be reduced by ≈2 orders of magnitude with respect to its typical value of 10^{20}–10^{21} Pa s. Regardless of the activation energy, more than 95% IBC can eventually sink downward with such a low reference viscosity. Another factor that can lead to a reduction of the reference viscosity is the presence of trapped melt since fractions of few percent are sufficient to reduce the viscosity by up to 1 order of magnitude. In addition, the

deformation of the lunar mantle could be controlled by nonlinear dislocation creep. At the typical strain rates of lunar mantle convection, in fact, the effective viscosity can be reduced by up to 3–4 orders of magnitude with respect to its typical values (Figure 2).

The rheology of the lunar mantle is still poorly constrained. In this work, the selection of reference viscosity and activation energy is based primarily on laboratory experiments on olivine. It is unknown whether these data are also representative for the lunar mantle. For the Moon, Zhang et al. (2013a) recommended a reference viscosity ranging from 5×10^{19} to 10^{21} Pa s at a reference temperature of 1300 °C (or nearly 1600 K), which can well reproduce the temperature of today's lunar mantle based on geodynamic modeling. This estimation supports the selection of reference viscosity in this work.

The low viscosity inferred from our models may not need to be representative of the entire mantle but only of ilmenite-rich materials. As a rheologically weak and nonlinear component in the ilmenite-olivine mixture, ilmenite can significantly reduce the viscosity of the IBC layer. Dygert et al. (2016) reported that the viscosity of ilmenite-olivine mixtures is 1 to 2 orders of magnitude lower than the viscosity of peridotite at temperatures between ≈1500 and 1700 K. Indeed, even with a reference viscosity of 10^{20} Pa s, the overturn of IBC is strongly facilitated if the viscosity of IBC is reduced by 1 order of magnitude with respect to that of the mantle (Figure 5c).

A rheologically weak IBC layer due to a nonlinear rheology requires the local strain rate to be sufficiently large. As shown in Figure 2, given the temperature of ilmenite crystallization (≈1400 K), the IBC layer is rheologically weaker with respect to the underlying lunar mantle if its local strain rate is higher than 6.4×10^{-16} s^{-1} for a reference viscosity of 10^{19} Pa s, 2.5×10^{-18} s^{-1} for a reference viscosity of 10^{20} Pa s, or 10^{-18} s^{-1} for a reference viscosity of 10^{21} Pa s. As the IBC layer could be trapped by the stagnant lid, a question is raised whether the strain rate in this region can be high enough to reduce the viscosity through nonlinear deformation. An analysis of our simulations indicates that strain rates necessary for dislocation creep to dominate could be reached for reference viscosities of 10^{20} Pa s or lower. For $\eta_r = 10^{21}$ Pa s instead, the strain rates we find are very low (of the order of 10^{-20} s^{-1}). At these conditions, diffusion creep would likely dominate and, as our results indicate, the overturn would not be possible. In this sense, we expect the need for a low reference viscosity to be a robust finding, independent of the use of linear or nonlinear rheologies.

The choice of the activation energy controls the viscosity contrast over the IBC layer and, in turn, also affects the development of the overturn. Our results suggest that a low activation energy strongly promotes the overturn. Even with $\eta_r = 10^{20}$ Pa s and $\Delta\eta_{\mathrm{IBC}} = 1$, we can still observe a significant overturn of IBC using an activation energy of 100 kJ/mol. Such a low effective activation energy, as discussed in Section 2, could be achieved by deformation via dislocation creep. Yet it must still be demonstrated with numerical models accounting for a mixed diffusion-dislocation creep rheology whether or not the dynamics of the overturn is governed by dislocation-dominated deformation and whether this can be reliably mimicked using a linear rheology with a reduced activation energy.

Parmentier et al. (2002) investigated the compositional—but isothermal—overturn of a dense IBC layer and inferred the conditions under which this can take place in the form of a degree-one downwelling. This is important because an overturn with long-wavelength pattern could be responsible for the accumulation of KREEP material beneath the Procellarum KREEP Terrane, which in turn could control the hemispherical production of partial melt that later leads to the generation of mare basalts (e.g., Laneuville et al., 2013). The authors concluded that the dense layer must be sufficiently thick (50–100 km) and have a viscosity at least 4 orders of magnitude lower than the underlying lighter layer in order for degree one to be the fastest growing wavelength of instability of the system. The thickness of the IBC layer is likely smaller than 50 km: 36 km according to our crystallization sequence (Figure 4a) and ≈30 km according to Hess and Parmentier (1995), or even less if a thinner magma ocean or a different composition are assumed (see section 3.1). Parmentier et al. (2002) argued that the overturn could actually begin with a small characteristic wavelength comparable to the IBC thickness. The large viscosity of the lighter underlying material would then prevent IBC diapirs from sinking rapidly and cause them to form a relatively thick and less dense layer of mixed IBC and mantle material, which could then satisfy the conditions for a degree-one overturn, provided that the IBC viscosity is at least 4 orders of magnitude lower than the viscosity of the underlying mantle.

In our simulations, we did not observe the overturn taking place with such a long wavelength. As illustrated in Figures 6 and 7, the compositional overturn is characterized by small-scale diapirs developing from the bottom of the IBC layer, a behavior that we observed in all cases where the overturn was possible. On the one hand, we accounted for a viscosity reduction of the IBC of only 1 order of magnitude (in line with the results of Dygert et al. (2016)). Since a higher viscosity contrast is nevertheless possible, on these grounds we cannot completely exclude the possibility of a low-degree instability. On the other hand, we did consider a strong temperature dependence of the viscosity whose effect is twofold. It causes the stagnant lid to grow rapidly, entrapping part of the IBC or at least retarding its mobilization (Figure 7), an effect that would be even more pronounced if the thickness of the IBC were lower than that used here. As a consequence, the effective thickness of the IBC available for the overturn tends to decrease. This renders it difficult to form a layer of dense material sufficiently thick for a degree-one instability to develop according to the mechanism proposed by Parmentier et al. (2002). Furthermore, the viscosity of the relatively hot, near-solidus mantle beneath the IBC tends to decrease rapidly with depth (Figure 5a). This makes the viscosity contrast of 10^4 between IBC and mantle, which is required for the development of a degree-one overturn, difficult to reach despite a possibly low viscosity of the IBC.

A limitation of our models is the choice of 2-D geometry (half cylinder with free-slip and insulating sidewalls), which was required in order to properly resolve the deformation of the thin IBC layer. The effects of a 3-D geometry could be twofold. On the one hand, Guerrero et al. (2018) recently compared simulations of stagnant lid convection carried out in 2-D spherical annuli (Hernlund & Tackley, 2008) and 3-D spherical shells. Particularly for small core-to-planet radius ratios such as that of the Moon, the authors showed that 2-D (statistical steady state) solutions systematically overestimate the mantle temperature. If this were actually the case despite the short time scale we dealt with in our study, our conclusions on the need of a weak lunar rheology would be strengthened. A cooler mantle would have a higher viscosity, which would ease the formation of the stagnant lid and hinder the IBC overturn. Therefore, even lower-reference viscosities or activation energies might be required. On the other hand, small cores tend to promote the formation of low-degree (possibly degree-one) structures in 3-D isochemical thermal convection (Guerrero et al., 2018; Yao et al., 2014). The IBC overturn is driven by a compositional instability, which, as previously discussed in this section, is likely to grow according to a small wavelength comparable to the IBC thickness. Yet this remains to be ultimately tested with high-resolution 3-D simulations of thermochemical convection.

6. Conclusions

By modeling the crystallization sequence of the LMO, we showed that a dense, 36-km-thick IBC layer forms beneath the plagioclase crust. Albeit gravitationally unstable, this layer tends to remain trapped in the stagnant lid, which grows rapidly because of the strong temperature dependence of the viscosity. We showed that the overturn of IBC is possible if the reference viscosity or activation energy are sufficiently low. A low viscosity allows rapid sinking of the IBC, while a low activation energy retards the growth of the stagnant lid, which allows more time for the overturn to develop. Considering a weak IBC further facilitates the overturn. An analysis in terms of scaling laws for Rayleigh-Taylor instability of plane layers of different densities and viscosities confirmed the above results.

For a reference viscosity of 10^{21} Pa s at ≈1600 K that is often assumed in mantle convection simulations, IBC overturn does not take place, independent of the choice of the other rheological parameters. The same conclusion applies to a reference viscosity of 10^{20} Pa s combined with a standard activation energy of 300 kJ/mol. For other combinations of reference viscosities and activation energies for which the IBC sink downward, we observe either partial or complete overturn. With $\eta_r = 10^{20}$ Pa s, a partial overturn needs an activation energy of 100–200 kJ/mol that could be achieved if the deformation was dominated by dislocation creep.

For a reference viscosity of 10^{18}–10^{19} Pa s, a complete overturn can take place regardless of the value of activation energy or whether or not the IBC are rheologically weak, which indicates the fundamental role of the reference viscosity in controlling the overturn of IBC. Such a weak rheology can be achieved with either a hydrated mantle, possibly in combination with the presence of trapped melt, or via dislocation creep. In future studies, the effects of dislocation creep and hydrous lunar mantle on the overturn of IBC will have to be investigated further.

Acknowledgments
We thank Scott King, Julian Lowman, and an anonymous reviewer whose comments helped to significantly improve an earlier version of the manuscript, and Steve Hauck for editorial handling. S. Yu and L. Xiao were supported by the Science and Technology Development Fund of Macau SAR (107/2014/A3 and 079/2018/A2). N. Tosi, M. Maurice, and S. Schwinger acknowledge support from the Helmholtz Association (grant VH-NG-1017). S. Schwinger and D. Breuer were also supported by the German Research Foundation (SFB-TRR 170). This is TRR publication 38. Computational time was provided by the HLRN (project bep00063), which is gratefully acknowledged. The data of numerical modeling and the scripts for generating the figures can be accessed at https://figshare.com/projects/LMO_overturn/35624.

References

Buck, W. R., & Toksoez, M. N. (1980). The bulk composition of the Moon based on geophysical constraints. *Proceedings of the Lunar and Planetary Science Conference*, *11*, 2043–2058.

Charlier, B., Grove, T., Namur, O., & Holtz, F. (2018). Crystallization of the lunar magma ocean and the primordial mantle-crust differentiation of the Moon. *Geochimica et Cosmochimica Acta*, *234*, 50–69.

Christensen, U. (1984). Convection with pressure-and temperature-dependent non-Newtonian rheology. *Geophysical Journal International*, *77*(2), 343–384.

Cisowski, S. M., Collinson, D. W., Runcorn, S. K., Stephenson, A., & Fuller, M. (1983). A review of lunar paleointensity data and implications for the origin of lunar magnetism. *Journal of Geophysical Research*, *88*, 691–704.

de Vries, J., van den Berg, A., & van Westrenen, W. (2010). Formation and evolution of a lunar core from ilmenite-rich magma ocean cumulates. *Earth and Planetary Science Letters*, *292*(1), 139–147. https://doi.org/10.1016/j.epsl.2010.01.029

Dygert, N., Hirth, G., & Liang, Y. (2016). A flow law for ilmenite in dislocation creep: Implications for lunar cumulate mantle overturn. *Geophysical Research Letters*, *43*, 532–540. https://doi.org/10.1002/2015GL066546

Elardo, S. M., Draper, D. S., & Shearer, C. K. (2011). Lunar magma ocean crystallization revisited: Bulk composition, early cumulate mineralogy, and the source regions of the highlands Mg-suite. *Geochimica et Cosmochimica Acta*, *75*(11), 3024–3045.

Elkins-Tanton, L. T., Burgess, S., & Yin, Q.-Z. (2011). The lunar magma ocean: Reconciling the solidification process with lunar petrology and geochronology. *Earth and Planetary Science Letters*, *304*, 326–336.

Elkins-Tanton, L. T., Van Orman, J. A., Hager, B. H., & Grove, T. L. (2002). Re-examination of the lunar magma ocean cumulate overturn hypothesis: Melting or mixing is required. *Earth and Planetary Science Letters*, *196*(3), 239–249.

Evans, A. J., Zuber, M. T., Weiss, B. P., & Tikoo, S. M. (2014). A wet, heterogeneous lunar interior: Lower mantle and core dynamo evolution. *Journal of Geophysical Research: Planets*, *119*, 1061–1077. https://doi.org/10.1002/2013JE004494

Garcia, R., Gagnepain-Beyneix, J., Chevrot, S., & Lognonné, P. (2011). Very preliminary reference Moon model. *Physics of the Earth and Planetary Interiors*, *188*(1–2), 96–113.

Ghiorso, M. S., Hirschmann, M. M., Reiners, P. W., & Kress, V. C. (2002). The pMELTS: A revision of MELTS for improved calculation of phase relations and major element partitioning related to partial melting of the mantle to 3 GPa. *Geochemistry, Geophysics, Geosystems*, *3*(5), 1030. https://doi.org/10.1029/2001GC000217

Guerrero, J., Lowman, J. P., Deschamps, F., & Tackley, P. (2018). The influence of curvature on convection in a temperature-dependent viscosity fluid: Implications for the 2-D and 3-D modeling of Moons. *Journal of Geophysical Research: Planets*, *123*, 1863–1880. https://doi.org/10.1029/2017JE005497

Harada, Y., Goossens, S., Matsumoto, K., Yan, J., Ping, J., Noda, H., & Haruyama, J. (2014). Strong tidal heating in an ultralow-viscosity zone at the core-mantle boundary of the Moon. *Nature Geoscience*, *7*, 569–572. https://doi.org/10.1038/ngeo2211

Hauri, E. H., Saal, A. E., Rutherford, M. J., & Orman, J. A. V. (2015). Water in the Moon's interior: Truth and consequences. *Earth and Planetary Science Letters*, *409*, 252–264.

Hernlund, J. W., & Tackley, P. J. (2008). Modeling mantle convection in the spherical annulus. *Physics of the Earth and Planetary Interiors*, *171*(1-4), 48–54.

Hess, P., & Parmentier, E. (1995). A model for the thermal and chemical evolution of the Moon's interior: Implications for the onset of mare volcanism. *Earth and Planetary Science Letters*, *134*(3), 501–514.

Hirth, G., & Kohlstedt, D. (2003). Rheology of the upper mantle and the mantle wedge: A view from the experimentalists. In G. Hirth & D. Kohlstedt (Eds.), *Inside the subduction Factory* (pp. 83–105). Washington, DC: American Geophysical Union.

Hood, L. L., & Jones, J. H. (1987). Geophysical constraints on lunar bulk composition and structure: A reassessment. *Journal of Geophysical Research*, *92*(B4), E396—E410.

Hüttig, C., Tosi, N., & Moore, W. (2013). An improved formulation of the incompressible Navier-Stokes equations with variable viscosity. *Physics of the Earth and Planetary Interiors*, *220*, 11–18. https://doi.org/10.1016/j.pepi.2013.04.002

Jordan, P. G. (1987). The deformational behaviour of bimineralic limestone-halite aggregates. *Tectonophysics*, *135*(1), 185–197.

Karato, S. I. (2013). Geophysical constraints on the water content of the lunar mantle and its implications for the origin of the Moon. *Earth and Planetary Science Letters*, *384*(13), 144–153.

Karato, S., & Wu, P. (1993). Rheology of the upper mantle: A synthesis. *Science*, *260*(5109), 771–778.

Kuskov, O. L., & Kronrod, V. A. (2001). Core sizes and internal structure of Earth's and Jupiter's satellites. *Icarus*, *151*(2), 204–227.

Kuskov, O. L., Kronrod, V. A., & Hood, L. L. (2002). Geochemical constraints on the seismic properties of the lunar mantle. *Physics of the Earth and Planetary Interiors*, *134*(3–4), 175–189.

Laneuville, M., Wieczorek, M. A., Breuer, D., Aubert, J., Morard, G., & Rückriemen, T. (2014). A long-lived lunar dynamo powered by core crystallization. *Earth and Planetary Science Letters*, *401*(401), 251–260.

Laneuville, M., Wieczorek, M., Breuer, D., & Tosi, N. (2013). Asymmetric thermal evolution of the Moon. *Journal of Geophysical Research: Planets*, *118*, 1435–1452. https://doi.org/10.1002/jgre.20103

Longhi, J. (2003). A new view of lunar ferroan anorthosites: Postmagma ocean petrogenesis. *Journal of Geophysical Research*, *108*(E8), 5083. https://doi.org/10.1029/2002JE001941

Morgan, J. W., Hertogen, J., & Anders, E. (1978). The Moon: Composition determined by nebular processes. *Moon and the Planets*, *18*(4), 465–478.

O'Neill, H. S. C. (1991). The origin of the Moon and the early history of the Earth—A chemical model. Part 1: The Moon. *Geochimica et Cosmochimica Acta*, *55*(4), 1159–1172.

Parmentier, E., Zhong, S., & Zuber, M. (2002). Gravitational differentiation due to initial chemical stratification: origin of lunar asymmetry by the creep of dense KREEP? *Earth and Planetary Science Letters*, *201*(3), 473–480.

Plesa, A.-C., Tosi, N., & Hüttig, C. (2012). Thermochemical convection in planetary mantles: Advection methods and magma ocean overturn simulations. In A.-C. Plesa, N. Tosi, & C. Hüttig (Eds.), *Integrated information and computing systems for natural, spatial, and social sciences* (pp. 302–323): IGI Global. https://doi.org/10.4018/978-1-4666-2190-9.ch015

Rapp, J., & Draper, D. (2018). Fractional crystallization of the lunar magma ocean: Updating the dominant paradigm. *Meteoritics & Planetary Science*, *53*(7), 1–24. https://doi.org/10.1111/maps.13086

Ringwood, A. E., & Kesson, S. E. (1976). A dynamic model for mare basalt petrogenesis. In *7th Lunar Science Conference* (Vol. 2, pp. 1697–1722). Houston, TX: Pergamon Press, Inc.

Saal, A. E., Hauri, E. H., Cascio, M. L., Van Orman, J. A., Rutherford, M. C., & Cooper, R. F. (2008). Volatile content of lunar volcanic glasses and the presence of water in the Moon's interior. *Nature*, *454*(7201), 192–195.

Scheinberg, A. L., Soderlund, K. M., & Elkins-Tanton, L. T. (2018). A basal magma ocean dynamo to explain the early lunar magnetic field. *Earth and Planetary Science Letters*, *492*, 144–151.
Shea, E. K., & Fuller, M. D. (2012). A long-lived lunar core dynamo. *Science*, *335*(6067), 453–456.
Smith, P. M., & Asimow, P. D. (2005). Adiabat_1ph: A new public front-end to the MELTS, pMELTS, and pHMELTS models. *Geochemistry, Geophysics, Geosystems*, *6*, Q02004. https://doi.org/10.1029/2004GC000816
Snyder, G. A., Taylor, L. A., & Neal, C. R. (1992). A chemical model for generating the sources of mare basalts: Combined equilibrium and fractional crystallization of the lunar magmasphere. *Geochimica et Cosmochimica Acta*, *56*(10), 3809–3823.
Stegman, D. R., Jellinek, M. A., Zatman, S. A., Baumgardner, J. R., & Richards, M. A. (2003). An early lunar core dynamo driven by thermochemical mantle convection. *Nature*, *421*, 143–146.
Stein, C., & Hansen, U. (2013). Arrhenius rheology versus Frank-Kamenetskii rheology—Implications for mantle dynamics. *Geochemistry, Geophysics, Geosystems*, *14*, 2757–2770. https://doi.org/10.1002/ggge.20158
Taylor, S. R. (1982). Planetary science: A lunar perspective (Vol. *3303*). Lunar and Planetary Science Institute.
Tosi, N., Grott, M., Plesa, A.-C., & Breuer, D. (2013). Thermochemical evolution of Mercury's interior. *Journal of Geophysical Research: Planets*, *118*, 2474–2487. https://doi.org/10.1002/jgre.20168
Tosi, N., Yuen, D. A., de Koker, N., & Wentzcovitch, R. M. (2013). Mantle dynamics with pressure- and temperature-dependent thermal expansivity and conductivity. *Physics of the Earth and Planetary Interiors*, *217*, 48–58. https://doi.org/10.1016/j.pepi.2013.02.004
Van Orman, J. A., & Grove, T. L. (2000). Origin of lunar high-titanium ultramafic glasses: Constraints from phase relations and dissolution kinetics of clinopyroxene-ilmenite cumulates. *Meteoritics and Planetary Science*, *35*(4), 783–794.
Wadhwa, M. (2008). Redox conditions on small bodies, the Moon and Mars. *Reviews in Mineralogy and Geochemistry*, *68*(1), 493–510.
Weber, R. C., Lin, P.-Y., Garnero, E. J., Williams, Q., & Lognonné, P. (2011). Seismic detection of the lunar core. *Science*, *331*(6015), 309–312.
Whitehead, J. A. (1988). Fluid models of geological hotspots. *Annual Review of Fluid Mechanics*, *20*(20), 61–87.
Wieczorek, M. A., Jolliff, B. L., Khan, A., Pritchard, M. E., Weiss, B. P., Williams, J. G., et al. (2006). The constitution and structure of the lunar interior. *Reviews in Mineralogy and Geochemistry*, *60*(1), 221–364.
Wieczorek, M. A., Neumann, G. A., Nimmo, F., Kiefer, W. S., Taylor, G. J., Melosh, H. J., et al. (2013). The crust of the Moon as seen by GRAIL. *Science*, *339*(6120), 671–675.
Yao, C., Deschamps, F., Lowman, J., Sanchez-Valle, C., & Tackley, P. (2014). Stagnant lid convection in bottom-heated thin 3-D spherical shells: Influence of curvature and implications for dwarf planets and icy moons. *Journal of Geophysical Research: Planets*, *119*, 1895–1913. https://doi.org/10.1002/2014JE004653
Zhang, N., Dygert, N., Liang, Y., & Parmentier, E. M. (2017). The effect of ilmenite viscosity on the dynamics and evolution of an overturned lunar cumulate mantle. *Geophysical Research Letters*, *44*, 6543–6552. https://doi.org/10.1002/2017GL073702
Zhang, N., Parmentier, E. M., & Liang, Y. (2013a). A 3-D numerical study of the thermal evolution of the Moon after cumulate mantle overturn: The importance of rheology and core solidification. *Journal of Geophysical Research: Planets*, *118*, 1789–1804. https://doi.org/10.1002/jgre.20121
Zhang, N., Parmentier, E. M., & Liang, Y. (2013b). Effects of lunar cumulate mantle overturn and megaregolith on the expansion and contraction history of the moon. *Geophysical Research Letters*, *40*, 5019–5023. https://doi.org/10.1002/grl.50988
Zhao, Y., van den Berg, A. P., & van Westrenen, W. (2016). in Lunar and planetary science conference (Vol. *47*, p. 1477).
Zhong, S., Parmentier, E. M., & Zuber, M. T. (2000). A dynamic origin for the global asymmetry of lunar mare basalts. *Earth and Planetary Science Letters*, *177*(3), 131–140.